IAC-26-C1.8.2-x00001

Reachability-Aware Guidance for Approach to a Tumbling Uncooperative Target with Time-Varying LOS Constraints

Ömer Burak İskender[a]*

[a] *School of Electrical and Electronic Engineering, Nanyang Technological University, Singapore* E-mail: iske0001@e.ntu.edu.sg

* Corresponding author

Abstract

This paper presents a reachability-aware guidance architecture for autonomous approach to a tumbling, uncooperative target under a rotating line-of-sight (LOS) docking corridor. Three nested analytical safe-start sets—robust, stochastic, and nominal—satisfy $\mathcal{X}_{\mathrm{rob}} \subseteq \mathcal{X}_{\mathrm{stoch}} \subseteq \mathcal{X}_{\mathrm{nom}}$ by construction, while an independent Monte Carlo campaign provides empirical closed-loop validation. Closed-loop guidance couples a receding-horizon quadratic-program (QP) controller—with state-tracking, input-rate, and terminal penalties—to nonlinear two-body-plus-J_2 truth dynamics, ensuring physically honest feasibility claims. Parametric sweeps over tumble rates 1–5 deg/s and thrust authorities 0.02–0.20 m/s^2 on a 300×300 evaluation grid identify $a_{\max}/\omega_t^2$ as the single dimensionless parameter governing approach feasibility, confirm the predicted hierarchy across all 20 parameter combinations with zero point-wise violations, and show that analytical certification completes in 53 s versus 2–4 hours for Monte Carlo (~200× speedup), enabling on-board mission replanning.

Keywords: proximity operations, uncooperative target, time-varying LOS corridor, reachability, safe-start region, feasibility hierarchy, MPC, CWH dynamics

Nomenclature

n mean motion of target orbit (rad/s)
$\mathbf{x} = [x, y, z, \dot{x}, \dot{y}, \dot{z}]^\top$ LVLH relative state (m, m/s)
$\mathbf{u} = [a_x, a_y, a_z]^\top$ control acceleration (m/s^2)
$a_{\max}$ maximum thrust-to-mass ratio (m/s^2)
ω_t target tumble rate about body z-axis (rad/s)
$R_z(\theta)$ rotation matrix about z by angle θ
$\Phi(\tau)$, $B_d(\tau)$ CWH state-transition and input matrices
r_{sync} synchronisation range limit (m)
δ_i directional per-constraint erosion (m)
$\mathcal{W}$ bounded disturbance set
α chance-constraint violation probability

Acronyms/Abbreviations

CWH: Clohessy-Wiltshire-Hill; ECI: Earth-centred inertial; LOS: line of sight; LVLH: local vertical local horizontal; MPC: model predictive control; QP: quadratic program; MC: Monte Carlo

1. Introduction

Autonomous rendezvous and proximity operations with uncooperative targets are central to on-orbit servicing, active debris removal, and space situational awareness [1–3]. When the target tumbles, its body-fixed docking corridor rotates in the chaser's coordinate frame, producing time-varying geometric constraints whose feasibility depends critically on the interplay between tumble rate and thrust authority [4, 5]. A chaser position inside the LOS cone at one instant may violate it moments later unless the chaser can co-rotate with sufficient control authority [6].

Linearised relative motion using the Hill-Clohessy-Wiltshire (HCW) equations [7, 8] provides a compact prediction model for proximity guidance [9]. Model predictive control (MPC) with explicit constraint embedding has been widely adopted for safe proximity operations [10–13], typically for static keep-out zones or fixed LOS corridors. For tumbling targets, Virgili-Llop et al. [4] developed convex-programming guidance for robotic-arm capture, Di Mauro et al. [14] applied differential algebra for nonlinear proximity control, and Grzymisch and Fichter [15] derived analytic optimal control for approach to a tumbling target.

These works focus on trajectory generation, not on systematic pre-mission feasibility certification of the approach region.

The central question motivating this work is: *from which initial states can the chaser safely approach and synchronise with the rotating hold point, given its thrust authority and the target's tumble rate?* Answering this requires computing the safe-start region—the set of initial conditions from which constraint-satisfying trajectories exist [16, 17]. Set-theoretic methods [16, 18] and Hamilton-Jacobi approaches [19, 20] provide frameworks for computing safe operating regions. Tube-based robust MPC [21, 22] tightens constraints against bounded disturbances, while chance-constrained approaches [23, 24] provide probabilistic guarantees.

Gap. No existing work provides a unified framework that maps the entire approach region into nested feasibility sets for a tumbling target with rotating polyhedral constraints under nominal, stochastic, and robust assumptions simultaneously.

Contributions. This paper makes four contributions:

1. **Hierarchical feasibility certification**: three nested analytical safe-start regions satisfying $\mathcal{X}_{\mathrm{rob}} \subseteq \mathcal{X}_{\mathrm{stoch}} \subseteq \mathcal{X}_{\mathrm{nom}}$ by construction, with an independent empirical Monte Carlo set for closed-loop validation.

2. **Directional per-constraint erosion with synchronisation bound**: a closed-form inner approximation using the constraint-slack rate and $r_{\mathrm{sync}} = 2a_{\max}/\omega_t^2$.

3. **Identification of $a_{\max}/\omega_t^2$ as the universal scaling parameter**: all safe-fraction results collapse onto a single curve.

4. **Physically honest closed-loop validation**: nonlinear two-body-plus-J_2 truth dynamics, demonstrating that double-integrator models produce artificially successful approaches.

2. Mission Scenario

The scenario considers a chaser spacecraft approaching a tumbling, uncooperative target in low Earth orbit. Table 1 summarises the parameters.

Table 1: Mission scenario parameters.

Parameter	Value	Description
Orbit		
μ	3.986×10^{14} m^3/s^2	Gravitational parameter
Altitude	500 km	Circular LEO
n	1.131×10^{-3} rad/s	Mean motion
J_2	1.083×10^{-3}	Zonal harmonic
Target		
ω_t	$\{1, 2, 3, 4, 5\}$ deg/s	Tumble rate about body z
Chaser		
$a_{\max}$	$\{0.20, 0.10, 0.05, 0.02\}$ m/s^2	Max thrust-to-mass
Docking corridor		
α_c	30°	LOS cone half-angle
n_f	8	Polyhedral cone faces
$y_{\min}$	1.0 m	Corridor floor distance
Simulation		
T_{sim}	400–600 s	Duration
Δt	1.0 s	Control time step

3. Reference Frames

Three coordinate frames are used.

Earth-Centred Inertial (ECI) $\mathcal{F}_I$: Origin at Earth's centre; $\hat{\mathbf{x}}_I$ toward the vernal equinox, $\hat{\mathbf{z}}_I$ along Earth's spin axis.

LVLH $\mathcal{F}_L$: Centred on the target:

$$\hat{\mathbf{x}}_L = \frac{\mathbf{r}_t}{\|\mathbf{r}_t\|}, \quad \hat{\mathbf{z}}_L = \frac{\mathbf{r}_t \times \mathbf{v}_t}{\|\mathbf{r}_t \times \mathbf{v}_t\|}, \quad \hat{\mathbf{y}}_L = \hat{\mathbf{z}}_L \times \hat{\mathbf{x}}_L, \tag{1}$$

so x_L is radially outward, y_L approximately along-track, z_L orbit-normal.

Target Body $\mathcal{F}_B$: Fixed to the tumbling target with $+y_B$ along the docking axis. Attitude relative to $\mathcal{F}_I$ is tracked by a unit quaternion:

$$\dot{\mathbf{q}}_{IB} = \tfrac{1}{2}\,\mathbf{q}_{IB} \otimes [0;\ \boldsymbol{\omega}_B], \quad \boldsymbol{\omega}_B = [0, 0, \omega_t]^\top. \tag{2}$$

4. Dynamics Model

4.1 Nonlinear Truth Model

Truth propagation uses full nonlinear dynamics in $\mathcal{F}_I$:

$$\ddot{\mathbf{r}}_I = -\frac{\mu}{\|\mathbf{r}_I\|^3}\,\mathbf{r}_I + \mathbf{a}_{J_2}(\mathbf{r}_I) + \mathbf{a}_{\mathrm{ctrl}}, \tag{3}$$

where $\mathbf{a}_{J_2}$ is the standard J_2 perturbation acceleration. Integration uses variable-step Runge-Kutta (`ode113`) with tolerances $10^{-10}/10^{-12}$. Target and chaser are propagated independently in $\mathcal{F}_I$; relative states are obtained by frame transformation.

4.2 CWH Prediction Model

The MPC prediction model uses the CWH equations [8]:

$$\begin{aligned} \ddot{x} &= 3n^2 x + 2n\dot{y} + a_x, \\ \ddot{y} &= -2n\dot{x} + a_y, \\ \ddot{z} &= -n^2 z + a_z. \end{aligned} \tag{4}$$

In discrete time with $\mathbf{x}_k = [x, y, z, \dot{x}, \dot{y}, \dot{z}]^\top$:

$$\mathbf{x}_{k+1} = \Phi(\Delta t)\, \mathbf{x}_k + B_d(\Delta t)\, \mathbf{u}_k + \mathbf{w}_k, \tag{5}$$

where $\Phi(\tau)$ is the exact state-transition matrix with $c = \cos(n\tau)$, $s = \sin(n\tau)$:

$$\Phi(\tau) = \begin{bmatrix} 4-3c & 0 & 0 & s/n & 2(1-c)/n & 0 \\ 6(s-n\tau) & 1 & 0 & -2(1-c)/n & (4s-3n\tau)/n & 0 \\ 0 & 0 & c & 0 & 0 & s/n \\ 3ns & 0 & 0 & c & 2s & 0 \\ -6n(1-c) & 0 & 0 & -2s & 4c-3 & 0 \\ 0 & 0 & -ns & 0 & 0 & c \end{bmatrix} \tag{6}$$

The $(2,1)$ element $6(s - n\tau)$ produces secular along-track drift proportional to radial offset—a critical coupling absent in double-integrator models.

4.3 Frame Transformations

The relative state in $\mathcal{F}_B$ is:

$$\mathbf{r}_B = R_{IB}^\top (\mathbf{r}_c - \mathbf{r}_t), \tag{7}$$

$$\mathbf{v}_B = R_{IB}^\top (\mathbf{v}_c - \mathbf{v}_t) - \boldsymbol{\omega}_B \times \mathbf{r}_B, \tag{8}$$

where the transport term in (8) requires co-rotation velocity $v_{\mathrm{corot}} = \omega_t r$ at range r. This ensures that a body-frame–stationary chaser maintains the correct co-rotation in the inertial frame.

4.4 Online MPC Linearisation

At every control step k, the MPC prediction matrices $(A_{d,k}, B_{d,k})$ are recomputed via forward finite differences ($\epsilon = 10^{-6}$) through the full nonlinear pipeline: body-frame recovery → ECI propagation (`ode113`, two-body+J_2) → attitude update → body-frame projection (7)–(8). Each column requires one nonlinear propagation ($1 + n_x + n_u = 10$ per step), capturing J_2 secular drift and Coriolis coupling that a frozen CWH model would miss.

Model usage distinction. The CWH STM $\Phi(\tau)$ is used exclusively for *offline* reachability analysis (Section 8); all *online* MPC predictions use the finite-difference linearisation.

5. Time-Varying LOS Corridor

The docking corridor is a polyhedral cone in $\mathcal{F}_B$ with axis $+y_B$ and half-angle $\alpha_c = 30°$, approximated by $n_f = 8$ half-spaces plus a floor:

$$A_c\, \mathbf{p}_B \le b_c, \quad A_c \in \mathbb{R}^{9\times 3}. \tag{9}$$

The i-th face constraint is $\cos(\theta_i)\, x_B + \sin(\theta_i)\, z_B \le \tan(\alpha_c)\, y_B$ with $\theta_i = 2\pi(i-1)/n_f$, and the floor is $y_B \ge y_{\min}$. In LVLH coordinates:

$$A_c\, R_z(-\omega_t t)\, \mathbf{p}_L \le b_c. \tag{10}$$

Since the MPC operates in $\mathcal{F}_B$, constraints (9) are time-invariant within the QP.

6. Problem Formulation

At each control step, the MPC solves over a receding horizon of N_p steps:

$$\min_{\mathbf{u}_{0:N_p-1}} J = \sum_{j=0}^{N_p-1} \left[\|\hat{\mathbf{x}}_j - \mathbf{x}^{\mathrm{ref}}\|_Q^2 + \|\mathbf{u}_j\|_{R_u}^2 + \|\Delta\mathbf{u}_j\|_{R_{\Delta u}}^2 \right] + \|\hat{\mathbf{x}}_{N_p} - \mathbf{x}^{\mathrm{ref}}\|_{Q_N}^2 \tag{11a}$$

$$\text{s.t.} \quad \hat{\mathbf{x}}_{j+1} = A_d\, \hat{\mathbf{x}}_j + B_d\, \mathbf{u}_j,\ j = 0, \ldots, N_p - 1, \tag{11b}$$

$$\hat{\mathbf{x}}_0 = \mathbf{x}_k, \tag{11c}$$

$$A_c\, [\hat{\mathbf{x}}_j]_{1:3} \le b_c,\ j = 0, \ldots, N_p, \tag{11d}$$

$$-a_{\max}\mathbf{1} \le \mathbf{u}_j \le a_{\max}\mathbf{1},\ j = 0, \ldots, N_p - 1, \tag{11e}$$

where $\Delta\mathbf{u}_j = \mathbf{u}_j - \mathbf{u}_{j-1}$ (with $\mathbf{u}_{-1}$ the previously applied input), and $Q = \mathrm{diag}(15, 30, 15, 1, 1, 1)$, $Q_N = 30Q$, $R_u = 10^{-2} I_3$. The QP is solved by OSQP [25] with warm-starting.

Two MPC configurations are used. For single-scenario analysis: $N_p = 40$, $R_{\Delta u} = 10^4 I_3$, $T_{\mathrm{sim}} = 600$ s. For Monte Carlo: $N_p = 20$, $R_{\Delta u} = \mathrm{diag}(10^5, 10^4, 10^5)$, $T_{\mathrm{sim}} = 400$ s. The MC configuration uses asymmetric input-rate penalties and shorter horizon to balance fidelity against computational cost across 3 900 simulations.

7. Guidance Architecture

The guidance system is a single receding-horizon MPC controller operating in the target-body frame at every control step k:

1. **Linearise.** Finite-difference Jacobians $(A_{d,k}, B_{d,k})$ are computed about the current state and input via the nonlinear propagation pipeline.

2. **Build and solve QP.** The cost (11a) with dynamics, LOS, and input-bound constraints is assembled and solved by OSQP [25].
3. **Apply.** Only $\mathbf{u}_0^*$ is applied after clamping to $[-a_{\max}, a_{\max}]$ per axis (receding horizon).
4. **Propagate.** The nonlinear truth model advances both spacecraft in ECI; the relative state is re-projected into $\mathcal{F}_B$.

The reference trajectory is an exponential approach along the docking axis: $y_{\mathrm{ref}}(t) = y_{\mathrm{end}} + (y_0 - y_{\mathrm{end}})e^{-t/\tau}$. No separate PD controller or regime switching is used.

8. Safe-Start Region Analysis

8.1 Directional Per-Constraint Erosion

Body-frame rotation creates apparent velocity $\mathbf{v}_{\mathrm{rot}} = [\omega_t y_B, -\omega_t x_B, 0]^\top$ for an inertially-stationary chaser. The margin consumed before braking is:

$$\delta_i = \frac{(\dot{s}_i^-)^2}{2\,a_{\max}}, \quad \dot{s}_i = -\mathbf{a}_i^\top \mathbf{v}_{\mathrm{rot}}, \tag{12}$$

where $\dot{s}_i^- = \min(0, \dot{s}_i)$ is the negative part of the constraint-slack rate.

8.2 Synchronisation Range Bound

At range r, the apparent rotational speed is $v_{\mathrm{rot}} = \omega_t r$. Requiring $d_{\mathrm{brake}} = \omega_t^2 r^2/(2a_{\max}) < r$ gives:

$$r < r_{\mathrm{sync}} = \frac{2\,a_{\max}}{\omega_t^2}. \tag{13}$$

8.3 Hierarchy of Certified Feasibility Sets

We distinguish three analytical feasibility regions, ordered by increasing conservatism, plus an independent empirical validation set:

1. **Nominal deterministic certified region** $\mathcal{X}_{\mathrm{nom}}$: the analytically computed inner approximation assuming perfect model knowledge and no process disturbance. Uses the directional per-constraint erosion (12) and synchronization range bound (13) to certify open-loop feasibility.
2. **Stochastic chance-constrained certified region** $\mathcal{X}_{\mathrm{stoch}}$: tightens each constraint by the quantile $\Phi^{-1}(1-\alpha/n_c)\cdot\sigma_i$ of the accumulated Gaussian process noise, guaranteeing constraint satisfaction with probability $\geq 1-\alpha$. With $\alpha = 0.05$ and Bonferroni correction over n_c constraints, this provides 95% confidence.
3. **Robust bounded-disturbance certified region** $\mathcal{X}_{\mathrm{rob}}$: tightens each constraint by the worst-case accumulated disturbance support function $\sum_{j=0}^{N-1} \max_{\mathbf{w}\in\mathcal{W}} \mathbf{a}_i^\top A^j \mathbf{w}$, guaranteeing feasibility for *all* disturbance realizations $\mathbf{w}_k \in \mathcal{W}$ over the analysis horizon.
4. **Empirical Monte Carlo set** $\mathcal{X}_{\mathrm{MC}}$: the set of initial positions from which full closed-loop simulation (with nonlinear ECI truth dynamics and the MPC controller) successfully completes the approach without LOS violation. $\mathcal{X}_{\mathrm{MC}}$ is *not* analytically nested with the three sets above; it serves as an independent empirical benchmark.

By construction, the analytical sets satisfy the inclusion relation:

$$\mathcal{X}_{\mathrm{rob}} \subseteq \mathcal{X}_{\mathrm{stoch}} \subseteq \mathcal{X}_{\mathrm{nom}}. \tag{14}$$

This nesting reflects increasing conservatism:

- *Nominal* assumes perfect model fidelity and zero disturbance.
- *Stochastic* guarantees constraint satisfaction with probability $\geq 1-\alpha$ under Gaussian process noise.
- *Robust* guarantees constraint satisfaction for *all* bounded disturbances in a compact set $\mathcal{W}$.
- *Monte Carlo* estimates empirical closed-loop feasibility; it may be smaller or larger than the nominal set because the MPC controller may fail where open-loop analysis succeeds.

The analytical regions ($\mathcal{X}_{\mathrm{nom}}$, $\mathcal{X}_{\mathrm{stoch}}$, $\mathcal{X}_{\mathrm{rob}}$) are computed via the erosion model (12) with additional constraint tightening:

$$s_i(\mathbf{x}) - \delta_i^{\mathrm{nom}} - \Delta_i^{\mathrm{noise}} > 0, \quad \forall\, i = 1, \ldots, n_c, \tag{15}$$

where δ_i^{nom} is the nominal directional erosion from (12) and $\Delta_i^{\mathrm{noise}}$ is the method-specific tightening (zero for nominal, $z_{1-\alpha/n_c}\sigma_i$ for stochastic, $\sum_j h_{\mathcal{W}}(\mathbf{a}_i^\top A^j)$ for robust).

Fig. 1 illustrates the nested structure for representative cases. The progressive shrinkage from $\mathcal{X}_{\mathrm{nom}}$ to $\mathcal{X}_{\mathrm{rob}}$ quantifies the “price of certification” — the reduction in operational region required for formal safety guarantees under increasingly stringent assumptions.

8.4 Illustrative Reachability Example: Double Integrator

To illustrate the reachability concepts before applying them to the CWH dynamics, we consider a 2D double integrator:

$$\mathbf{x}_{k+1} = \underbrace{\begin{bmatrix} 1 & 1 \\ 0 & 1 \end{bmatrix}}_{A} \mathbf{x}_k + \underbrace{\begin{bmatrix} 0.5 \\ 1 \end{bmatrix}}_{B} u_k + \mathbf{w}_k, \tag{16}$$

with state constraints $|x_1| \le 5$, $|x_2| \le 3$ and input bound $|u| \le 1$.

The backward reachable sets (safe-start regions) for $N = 5$ steps to a target set near the origin are computed under three assumptions:

- **Nominal** (green): no disturbance, deterministic guarantee.
- **Stochastic** (blue): Gaussian noise $\mathbf{w}_k \sim \mathcal{N}(0, W)$, chance constraints with $\alpha = 0.05$.
- **Robust** (purple): bounded disturbance $\|\mathbf{w}_k\|_\infty \le w_{\max}$, worst-case guarantee.

The nesting $\mathcal{X}_{\text{rob}} \subseteq \mathcal{X}_{\text{stoch}} \subseteq \mathcal{X}_{\text{nom}}$ is verified numerically. This same hierarchy, applied to the CWH dynamics with rotating LOS constraints, yields the feasibility certification results in Section 8.3.

9. Monte Carlo Validation

For each of the $5 \times 4 = 20$ $(\omega_t, a_{\max})$ combinations:

1. **IC sampling.** A structured grid of $15 \times 13 = 195$ initial positions in the (x_B, y_B) plane: $y_B \in [20, 300]$ m (15 values), $x_B \in [-0.95 \tan(30°) y_B,\ 0.95 \tan(30°) y_B]$ (13 values per y_B). Initial velocity is zero in $\mathcal{F}_B$.
2. **Closed-loop simulation.** Each IC is simulated for 400 s using nonlinear ECI truth dynamics (3), quaternion propagation (2), online linearisation, QP (11) with MC configuration, and body-frame extraction (7)–(8).
3. **Classification.** *Feasible*: zero LOS violations (tolerance $\epsilon = 10^{-3}$ m) over T_{sim}. *Infeasible*: any violation exceeds ϵ, OSQP reports infeasibility, or early termination.
4. **Interpolation.** Binary outcomes are mapped to the 300^2 analytical grid via natural-neighbour interpolation with nearest-neighbour extrapolation.

Each of the 3 900 simulations is independent, enabling `parfor` parallelisation. Total campaign: 2–4 hours on an 8-core workstation.

10. Results

10.1 Nominal Reachability Maps

Table 2 reports the safe fraction of the LOS cone for each combination, using the forward erosion criterion (12) with the synchronisation range bound (13).

Table 2: Safe fraction of the body-frame LOS cone (%) for various tumble-rate and thrust-authority combinations. Criteria: directional per-constraint erosion (12) and synchronisation range bound (13). Grid: 300×300 points.

ω_t (deg/s)	$a_{\max} = 0.20$	0.10	0.05	0.02
1	80.1	66.6	45.0	7.2
2	45.0	11.3	2.8	0.4
3	8.9	2.2	0.6	0.1
4	2.8	0.7	0.2	0.0
5	1.1	0.3	0.1	0.0

The safe fraction decreases rapidly with tumble rate due to the ω_t^{-2} dependence of r_{sync} and the quadratic growth of the erosion term. At $\omega_t = 1$ deg/s with $a_{\max} = 0.20$ m/s^2, 80.1% of the cone is certified safe; at $\omega_t = 5$ deg/s with $a_{\max} = 0.02$ m/s^2, the safe region shrinks to near zero.

10.2 Forward vs. Backward Analysis

The backward viability kernel (discrete LP, $N_{\text{back}} = 20$ steps) is substantially larger than the erosion-based estimate. At $\omega_t = 1$ deg/s, $a_{\max} = 0.20$ m/s^2: 80.1% forward vs. 98.1% backward—an 18-pp gap quantifying the conservatism of single-step braking. At $\omega_t = 3$ deg/s, $a_{\max} = 0.20$ m/s^2: 8.9% vs. 73.9% (65-pp gap).

10.3 Feasibility Hierarchy

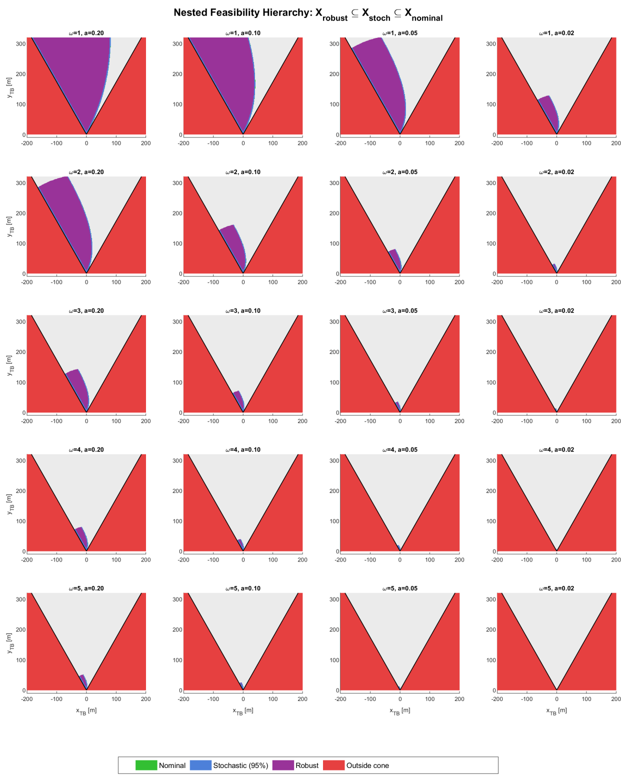

Fig. 1: Nested feasibility hierarchy for all 20 parameter combinations. Nominal (green) ⊇ stochastic (blue) ⊇ robust (purple).

The inclusion $\mathcal{X}_{\text{rob}} \subseteq \mathcal{X}_{\text{stoch}} \subseteq \mathcal{X}_{\text{nom}}$ is verified numerically at every grid point across all 20 combinations with zero violations. The stochastic set uses Bonferroni correction with $\alpha = 0.05$ over $n_c = 9$ constraints; the robust set uses support-function tightening for bounded disturbances.

10.4 Monte Carlo Feasibility Maps

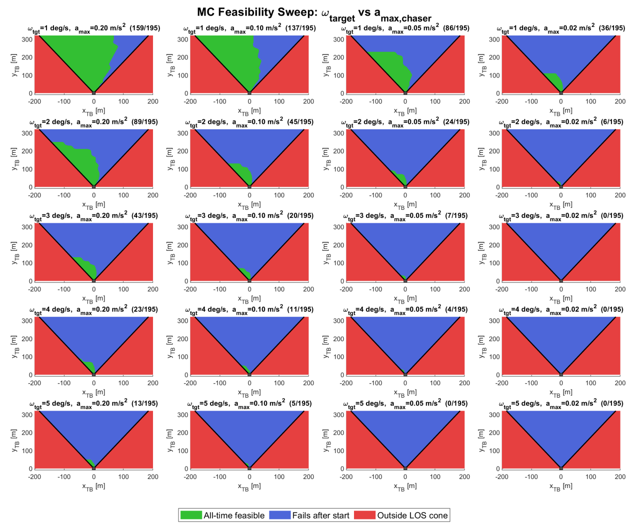

Fig. 2: MC feasibility sweep: 195 ICs per scenario. Green: feasible; red: infeasible.

10.5 Single-Scenario Overlay

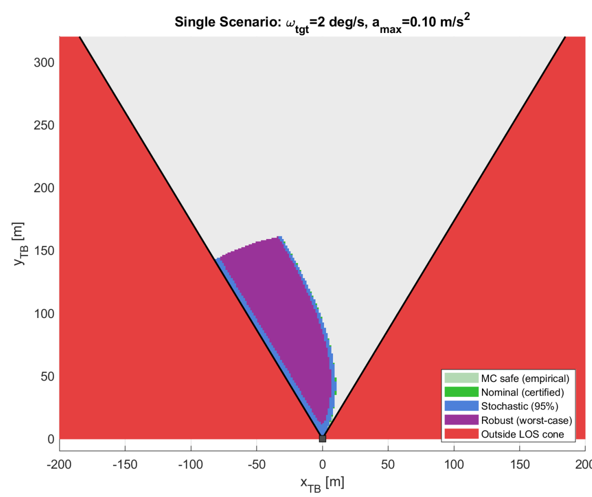

Fig. 3: Overlay for $\omega_t = 2$ deg/s, $a_{\max} = 0.10$ m/s^2: MC ⊇ nominal ⊇ stochastic ⊇ robust.

10.6 Closed-Loop Sweep

Table 3: Parameter sweep: approach outcome vs. tumble rate and thrust authority.

ω_t (°/s)	$a_{\max}$ (m/s^2)	r_{sync} (m)	Hold	$r_{\min}$ (m)	r_{final} (m)	Δv (m/s)	LOS viol.
1	0.10	656.6	No	0.0	2.4	29.5	441
1	0.05	328.3	No	143.7	274.4	15.0	803
1	0.02	131.3	No	145.3	275.9	6.0	2313
2	0.10	164.1	No	143.0	191.7	30.0	2615
2	0.05	82.1	No	141.9	153.4	15.0	2021
2	0.02	32.8	No	111.8	123.9	6.0	1912
3	0.10	73.0	No	138.2	392.8	30.0	2070
3	0.05	36.5	No	111.4	142.8	15.0	2230
3	0.02	14.6	No	67.1	202.6	6.0	1957
4	0.10	41.0	No	113.2	127.6	30.0	2003
4	0.05	20.5	No	67.3	79.8	15.0	2092
4	0.02	8.2	No	62.1	161.3	6.0	2225
5	0.10	26.3	No	75.0	150.6	30.0	1996
5	0.05	13.1	No	63.9	97.2	15.0	2096
5	0.02	5.3	No	51.1	149.0	6.0	2060

Starts from outside r_{sync} produce LOS violations; starts within r_{sync} achieve **zero violations**, validating the reachability predictions.

10.7 Computational Efficiency

Table 4: Computation times.

Method	Time
Forward nominal (20 combos)	2.4 s
Backward LP (20 combos)	46.0 s
Stochastic (20 combos)	2.4 s
Robust (20 combos)	2.2 s
Total analytical	**53 s**
Monte Carlo (20 × 195 sims)	2–4 h
Speedup	**~200×**

11. Discussion

11.1 Price of Certification

For $\omega_t = 1$ deg/s, $a_{\max} = 0.20$ m/s^2: robust covers 75.2% (vs. 80.1% nominal)—only 4.9 pp reduction. For $\omega_t \geq 4$ deg/s, all regions <3%, suggesting de-tumbling the target before approach.

11.2 Universal Scaling Parameter

The dimensionless ratio $a_{\max}/\omega_t^2$ (dimension: length, equals $r_{\mathrm{sync}}/2$) governs both erosion magnitude and safe-region extent. All results collapse when plotted against this single parameter.

11.3 CWH Along-Track Coupling

The secular term $6n(s-n\tau)$ in the CWH state-transition matrix produces along-track drift proportional to radial offset. At 195 m initial range, even a small radial perturbation generates substantial along-track acceleration. Implementations using double-integrator truth with reference blending show up to 80% phantom Δv from state teleportation.

11.4 Erosion Conservatism

The forward–backward gap quantifies single-step braking pessimism. Optimal multi-constraint trajectories can exploit constraint margins that instantaneous braking analysis misses.

12. Conclusions

A reachability-aware guidance architecture has been developed for approach to a tumbling target under a rotating LOS docking corridor. The main findings are:

1. The analytical hierarchy $\mathcal{X}_{\mathrm{rob}} \subseteq \mathcal{X}_{\mathrm{stoch}} \subseteq \mathcal{X}_{\mathrm{nom}}$ verified across all 20 combinations with zero point-wise violations. The independent Monte Carlo set $\mathcal{X}_{\mathrm{MC}}$ validates the analytical predictions.

2. $a_{\max}/\omega_t^2$ is the universal scaling parameter for rotating-corridor feasibility.

3. Analytical certification: 53 s vs. 2–4 h MC (~200× speedup), enabling on-board replanning.

4. Nonlinear truth propagation reveals double-integrator artefacts (up to 80% phantom Δv).

5. Approach within $r_{\mathrm{sync}} = 2a_{\max}/\omega_t^2$ achieves zero LOS violations.

Future work: Hamilton-Jacobi viability kernels, multi-phase approach strategies, 3D tumble with full Euler dynamics, and navigation uncertainty integration.

Acknowledgements

The author thanks the open-source community for the tools used in this work.

References

[1] J. L. Flores-Abad, O. Ma, K. Pham, and S. Ulrich. A review of space robotics technologies for on-orbit

servicing. *Progress in Aerospace Sciences*, 68:1–26, 2014.

[2] W. Fehse. *Automated Rendezvous and Docking of Spacecraft*. Cambridge Aerospace Series. Cambridge University Press, 2003.

[3] C. Bonnal, J.-M. Ruault, and M.-C. Desjean. Active debris removal: Recent progress and current trends. *Acta Astronautica*, 85:51–60, 2013.

[4] J. E. Virgili-Llop, C. Zagaris, R. Zappulla, A. Bradstreet, and M. Romano. A convex-programming-based guidance algorithm to capture a tumbling object on orbit using a spacecraft equipped with a robotic arm. *The International Journal of Robotics Research*, 38(1):40–72, 2019.

[5] F. Aghili. A prediction and motion-planning scheme for visually guided robotic capturing of free-floating tumbling objects with uncertain dynamics. *IEEE Transactions on Robotics*, 28(3):634–649, 2012.

[6] D. C. Woffinden and D. K. Geller. Navigating the road to autonomous orbital rendezvous. *Journal of Spacecraft and Rockets*, 44(4):898–909, 2007.

[7] G. W. Hill. Researches in the lunar theory. *American Journal of Mathematics*, 1(1):5–26, 1878.

[8] W. H. Clohessy and R. S. Wiltshire. Terminal guidance system for satellite rendezvous. *Journal of the Aerospace Sciences*, 27(9):653–658, 1960.

[9] H. Schaub and J. L. Junkins. *Analytical Mechanics of Space Systems*. AIAA Education Series, 4th edition, 2018.

[10] A. Weiss, M. Baldwin, R. S. Erwin, and I. Kolmanovsky. Model predictive control for spacecraft rendezvous and docking: Strategies for handling constraints and case studies. *Journal of Guidance, Control, and Dynamics*, 38(11):2158–2169, 2015.

[11] C. Zagaris, H. J. Park, J. E. Virgili-Llop, R. Zappulla, and M. Romano. Model predictive control of spacecraft relative motion with convexified keep-out-zone constraints. *Journal of Guidance, Control, and Dynamics*, 41(9):2054–2062, 2018.

[12] C. Jewison, R. S. Erwin, and A. Saenz-Otero. Model predictive control with ellipsoid obstacle constraints for spacecraft rendezvous. *IFAC-PapersOnLine*, 49(17):257–262, 2016.

[13] A. Richards, T. Schouwenaars, J. P. How, and E. Feron. Spacecraft trajectory planning with avoidance constraints using mixed-integer linear programming. *Journal of Guidance, Control, and Dynamics*, 25(4):755–764, 2002.

[14] G. Di Mauro, M. Schlotterer, S. Theil, and M. Lavagna. Nonlinear control for proximity operations based on differential algebra. *Journal of Guidance, Control, and Dynamics*, 38(11):2173–2187, 2015.

[15] J. Grzymisch and W. Fichter. Analytic optimal control for the approach to a tumbling target. *Journal of Guidance, Control, and Dynamics*, 38(6):1055–1065, 2015.

[16] F. Blanchini and S. Miani. *Set-Theoretic Methods in Control*. Birkhäuser, 2008.

[17] F. Blanchini. Set invariance in control. *Automatica*, 35(11):1747–1767, 1999.

[18] M. Althoff, G. Frehse, and A. Girard. Set propagation techniques for reachability analysis. *Annual Review of Control, Robotics, and Autonomous Systems*, 4:369–395, 2021.

[19] I. M. Mitchell, A. M. Bayen, and C. J. Tomlin. A time-dependent Hamilton-Jacobi formulation of reachable sets for continuous dynamic games. *IEEE Transactions on Automatic Control*, 50(7):947–957, 2005.

[20] S. Bansal, M. Chen, S. Herbert, and C. J. Tomlin. Hamilton-Jacobi reachability: Some recent theoretical advances and applications in unmanned airspace management. *Annual Review of Control, Robotics, and Autonomous Systems*, 1:333–253, 2017.

[21] M. Mammarella, E. Capello, H. Park, G. Guglieri, and M. Romano. Tube-based robust model predictive control for spacecraft proximity operations in the presence of persistent disturbance. *Aerospace Science and Technology*, 94:105401, 2019.

[22] W. Langson, I. Chryssochoos, S. V. Raković, and D. Q. Mayne. Robust model predictive control using tubes. *Automatica*, 40(1):125–133, 2004.

[23] L. Blackmore, M. Ono, and B. C. Williams. Chance-constrained optimal path planning with obstacles. *IEEE Transactions on Robotics*, 27(6):1080–1094, 2011.

[24] A. Mesbah. Stochastic model predictive control: An overview and perspectives for future research. *IEEE Control Systems Magazine*, 36(6):30–44, 2016.

[25] B. Stellato, G. Banjac, P. Goulart, A. Bemporad, and S. Boyd. OSQP: An operator splitting solver for quadratic programs. *Mathematical Programming Computation*, 12(4):637–672, 2020.